

pubs.acs.org/crystal Article

# Optimization of PbTiO<sub>3</sub> Single Crystals with Flux and Laser Floating Zone Method

Lucas A. Pressley,\* Mekhola Sinha, Hector K. Vivanco, Juan Chamorro, Sujit Das, Ramamoorthy Ramesh, and Tyrel M. McQueen\*



Cite This: Cryst. Growth Des. 2022, 22, 5629-5638



**ACCESS** 

Metrics & More

ABSTRACT: PbTiO<sub>3</sub> is an established high temperature ferroelectric and component of multiferroic devices. Single crystal growth of clean PbTiO<sub>3</sub> has largely been limited to flux growth, in part due to the volatility of PbTiO<sub>3</sub> near the melting point. We demonstrate the ability to grow single crystals of PbTiO<sub>3</sub> using the laser diode floating zone technique. Crystal quality is examined using Laue, powder, and single crystal X-ray diffraction. Low temperature specific heat and annealing experiments using thermogravimetric analysis/differential thermal

annealing experiments using thermogravimetric analysis/differential thermal analysis were used to compare the disorder and vacancies generated in the laser diode floating zone with those produced by flux growth. Samples grown using the floating zone method showed minimal oxygen deficiency, while samples grown via flux had a higher density of vacancies and metal impurities (determined using glow discharge mass spectrometry), resulting in room temperature ferromagnetic

behavior. The use of laser diodes as a heating source in the optical floating zone technique is essential in the stability of the zone growth and could be applied for production and zone refinement of other volatile materials.

PbTio<sub>3</sub>
PbTio<sub>3</sub>
PbTio<sub>3</sub>
PbTio<sub>4</sub>
PbTi<sub>1</sub>
PbTi<sub>2</sub>
PbTi<sub>3</sub>
PbTio<sub>4</sub>
PbTi<sub>2</sub>
PbTi<sub>3</sub>
PbTio<sub>5</sub>
PbTio<sub>5</sub>
PbTio<sub>6</sub>
PbTio<sub>6</sub>
PbTio<sub>7</sub>
PbTio<sub>7</sub>
PbTio<sub>8</sub>
PbTio<sub>8</sub>
PbTio<sub>8</sub>
PbTio<sub>9</sub>

Article Recommendations

### ■ INTRODUCTION

Multiferroics, materials that exhibit two or more types of ordering below their corresponding Curie temperatures, are a highly desired class of materials due to their impact as potential memory devices. 1,2 Of particular interest is the coupling between systems that demonstrate ferromagnetism and ferroelectricity. The perovskite family has served as a useful structure in designing multiferroics, as many already exhibit one of the features needed to be classified as such.<sup>3,4</sup> The use of Er as a dopant has been pursued in designing multiferroics to improve its ferroelectric properties (see BiFeO<sub>3</sub> as an example). Er<sup>3+</sup> is also a prospective dopant for use in quantum information processing due to its optical transition around 1550 nm.6 Lone pair sterically active materials are often pursued due to the structural distortion present that gives rise to ferroelectricity. Thus, PbTiO<sub>3</sub> has been an important compound due to its high Curie temperature and ability to be incorporated with other materials and systems.<sup>8,9</sup> Prior reports of single crystal growth of different solid solutions involving PbTiO<sub>3</sub> have used a variety of techniques. 10-15 Most reports of crystals use the flux method. 16-19 The floating zone technique is useful in preparing low defect single crystals due to being crucible-free. It further has the benefit of purifying the material by zone refinement.<sup>20</sup> Works reporting using a floating zone furnace for PbTiO<sub>3</sub> had very fast growth speeds (100 mm/h) and were largely unsuccessful due to the evaporation of PbO leading to an unstable, collapsing zone.<sup>21</sup> Recent progress in

the use of laser diode floating zone (LDFZ) furnaces in synthesizing a wide variety of materials, 22-25 including those with high vapor pressures, 26-28 encourages revisitation of this technique as applied to PbTiO<sub>3</sub>. Here we report the growth of bulk crystals (4 cm length, ~5 mm OD) of PbTiO<sub>3</sub> using the LDFZ. The presence of oxygen vacancies is quantified using thermogravimetric analysis/differential thermal analysis (TGA/DTA) and shows that the floating zone grown samples have fewer vacancies as prepared. Impurity metal concentrations are estimated from magnetization measurements and glow discharge mass spectrometry (GDMS). The presence of impurity driven room temperature ferromagnetism in flux grown crystals of PbTiO3, absent in LDFZ specimens, demonstrates the positive impacts of zone refinement and crucible-free techniques. Analysis of the low temperature heat capacity is also performed to probe the degree of structural disorder that is present. We see the expected off-centering of Pb through the fitting of the data to a series of phonon modes which serves as an explanation to previously suspect linear behavior at low temperatures. Overall, this comparison shows

Received: June 25, 2022 Revised: July 25, 2022 Published: August 3, 2022





Crystal Growth & Design pubs.acs.org/crystal Article

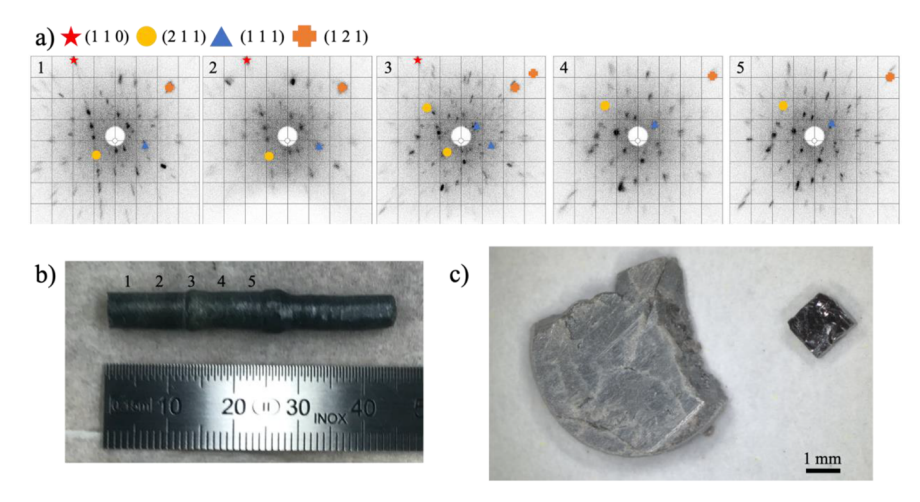


Figure 1. (a) Series of Laue images, taken along the length of the sanded crystal, demonstrating multiple grains. Key orientations are symbolized to help one keep track of crystal reorientation, happening at pattern 3. (b) As-grown crystal of Er-doped PbTiO<sub>3</sub> with the region labeled according to the section examined by Laue diffraction. (c) Piece of floating zone grown PbTiO<sub>3</sub> (left) compared to a crystal grown using PbO flux (right).

the usefulness of the LDFZ in growing low defect crystals of volatile materials through zone refinement as well as being crucible-free.

#### METHODS

The flux growth for PbTiO<sub>3</sub> is adapted from the double crucible procedure of Sun et al. 16 PbO (Alfa Aesar 99.9%, Lot No. B11T020) and TiO<sub>2</sub> (Alfa Aesar, 99.8% metals basis, Lot No. T05D048) were weighed in a 4:1 molar ratio. Materials were mixed in an agate mortar and pestle and loaded into a Pt crucible with a Pt lid. Mortar, pestle, and Pt crucible were cleaned before use with 1 M HCl(aq), rinsed with deionized water, and baked at  $T\sim 100~^{\circ}\mathrm{C}$  in efforts to avoid potential contamination, especially from iron. The crucible was then placed in an alumina boat, surrounded with TiO2 powder, and a second alumina boat was placed upside down to serve as another lid to reduce PbO evaporation. The double crucible was placed into a tube furnace and heated to  $T\sim 1100~^{\circ}\text{C}$  over 10 h, where it dwelled for 16 h; quickly cooled to  $T \sim 1050$  °C over 1 h; and then slowly cooled to 930 °C at a rate of 0.5 °C/h, at which point it cooled to room temperature over an additional 10 h. The leftover flux was removed by sonicating in 2 M acetic acid, leaving behind rectangular crystals on average  $2 \times 1 \times 1$  mm<sup>3</sup> in size.

PbTiO<sub>3</sub> powder (Alfa Aesar, 99.9% metals basis, Lot No. X15G039) was compacted into rod shapes using rubber balloons, evacuated, and subsequently subjected to hydrostatic pressure (~75 MPa). Upon removal from the balloon, the rods were sintered in an open alumina boat in a box furnace at  $T\sim 1000$  °C for 2 h. The sintered rods were mounted in a laser diode floating zone (LDFZ) furnace (Crystal Systems, Inc., FD-FZ-5-200-VPO-X PC) with 5 × 200 W GaAs lasers ( $\lambda$  = 976 nm); the seed rod was affixed to an alumina holder on the lower shaft using Nichrome wire, while the feed rod was suspended from a hook on the upper shaft using Nichrome wire. An applied pressure of 7.5 bar of Ar (g) was used flowing at 2 L/min with lasers tilted at 5° above the horizontal plane. The seed rod was melted, and the feed rod was joined to create a stable molten zone. Both rods were translated downward through the hot zone. The steady state conditions were found to occur when the upper and lower shaft traveled at rates of 13 and 10 mm/h, while counterrotating at 10 and 20 rpm, respectively.

PbTi<sub>0,99</sub>Er<sub>0,01</sub>O<sub>3</sub> samples were doped by mixing the aforementioned PbTiO<sub>3</sub> and PbO powders with previously dried Er<sub>2</sub>O<sub>3</sub> powder in an agate mortar and pestle. The powder was compacted into rods and sintered following the same procedure as the undoped samples. In these floating zone growths, growth conditions occurred as mentioned above except for the upper and lower shafts translating at 13.5 mm/h and 7 mm/h, respectively. For both sets of samples, after the first

initial growth, a portion of the as-grown crystal was used as the seed for subsequent growths.

Crystal orientation was determined using backscattered X-ray Laue diffraction with a tungsten source operating at 10 kV and 10 mA with a Multiwire Laboratories MWL 110 real-time back-reflection Laue camera. Laboratory-based X-ray diffraction patterns of the ground up single crystals were collected using a Bruker D8 Focus diffractometer with Cu K $\alpha$  radiation and a LynxEye detector. Rietveld refinements to check phase purity were performed using Bruker TOPAS software (Version 4.2, Bruker AXS). Single crystal X-ray diffraction were collected on a Bruker-Nonius X8 Proteum (Mo K $\alpha$  radiation) diffractometer using CrysAlisPro 1.171.41.93a (Rigaku Oxford Diffraction, 2020). Structure solution/refinement was performed using the WinGX software package. The structures were solved by Patterson methods using DIRDIF, followed by least-squares refinement using SHELXL-97. After initial refinements an empirical absorption correction was used, with spherical harmonics implemented in SCALE3 ABSPACK scaling algorithm, with weighting schemes applied near the end of refinement.<sup>30</sup> Attempts to refine occupancy of Pb or Ti sites resulted in no significant improvement in fit and as such were fixed at 1.

Heat capacity measurements from  $T=2-300~{\rm K}$  were taken with a Quantum Design physical properties measurement system (PPMS) using the semi-adiabatic pulse method with a 1% temperature rise. Magnetization data were collected as a function of field from -7 to 7 T on unaligned crystals using a Quantum Design magnetic property measurement system (MPMS). Simultaneous thermogravimetric analysis/differential thermal analysis (TGA/DTA) was done using a TA Instruments Q600 SDT. Crystals of both flux and floating zone grown samples (10–20 mg) were loaded in alumina pans and reacted under flowing  $O_2$  (25 mL/min). Samples were heated at a rate of 2 °C/min to 800 °C and held there for approximately 4 h. The mass change during oxidation was calculated by comparing the sample mass observed after holding at 150 °C for 1 h to sample mass after annealing at 800 °C to avoid errors associated with buoyancy or with surface-adsorbed moisture.

GDMS to determine trace elements was performed by Evans Analytical Group on both a floating zone grown and flux grown crystals of PbTiO<sub>3</sub>. Sample surface and composition from the cross-section of the undoped PbTiO<sub>3</sub> crystals grown using floating zone were probed using a JEOL JSM IT100 scanning electron microscope (SEM) at 20 keV operating in backscatter mode.

# RESULTS

**Crystal Growth.** Due to the volatility of  $PbTiO_3$ , stabilization of the floating zone was achieved by (1) applying

inert gas in the system, (2) using a faster travel rate than those for other materials, and (3) utilizing laser diodes as the heating source. It has been shown in previous crystal growths of volatile materials that using inert gas at elevated pressures has been successful in reducing the evaporation. 31,32 Here we noticed a visible reduction of volatilization occurred when applying  $Ar_{(g)}$  at 7.5 bar of pressure. A faster travel rate is often used in floating zone growths to reduce the amount of time any part of the sample is liquid if the material decomposes upon melting. This must be empirically balanced with a slow enough rate for crystallization to occur but has been demonstrated using growth speeds similar to those used here.<sup>33</sup> The use of laser diodes as a heating source significantly reduces the volume of the molten zone compared to conventional 4 mirror optical furnaces to approximately 1 mm in length zone with an average temperature gradient of 150 °C/mm.<sup>22</sup> This has the benefits of both an easier to maintain molten zone and reduction of the volatility, as demonstrated in other systems utilizing laser diodes.<sup>26</sup>

Through the combination of these parameters, we were able to achieve a stable zone resulting in samples  $\sim$ 5 mm diameter by 4 cm length. Laue diffraction performed on both Er-doped and stoichiometric PbTiO<sub>3</sub> to confirm crystal quality initially shows no signal; however, upon removal of an amorphous surface, we see clear spots, as demonstrated for the Er-doped sample in Figure 1a. Indexing of the pattern along the length shows a slight reorientation occurs when crystal shape changes. The doubled spots are indicative of twinning, expected for a crystal grown above the cubic to tetragonal phase transition temperature of  $T \sim 490$  °C. An Er-doped floating zone crystal measured along its length is shown in Figure 1b, with a cross-section of the undoped crystal shown in Figure 1c compared to the crystal grown via flux.

Analysis of the cross-section using SEM gives us insight as to how the material loss via volatization affects the grown crystal. A combination of backscattered electron imaging and energy dispersive spectroscopy (EDS) shows that PbO loss causes the formation of  ${\rm TiO_2}$  that shows up preferentially as inclusions, shown in Figure 2. We see that while PbO loss is

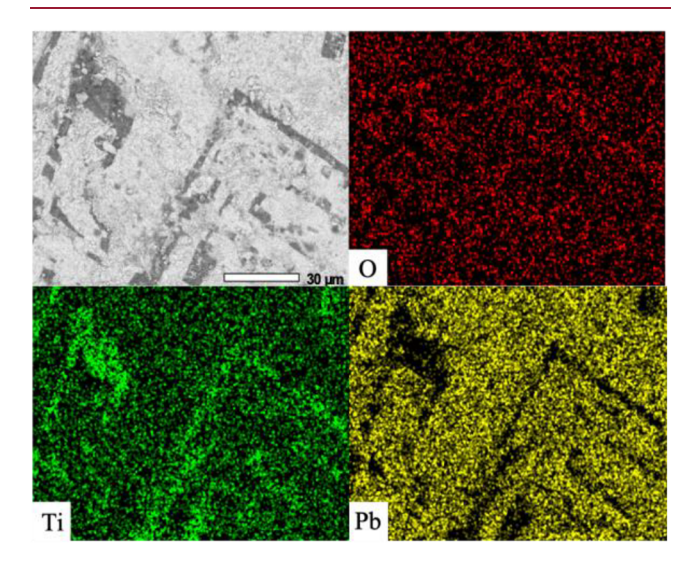


**Figure 2.** SEM backscattered image of the cross-section of floating zone grown  $PbTiO_3$  with EDS elemental maps showing the areas of Pb deficiencies.  $TiO_2$  regions show up as inclusions with crystalline shapes.

reduced using methods mentioned above such that stable growth is possible, defect formation is still possible. Further, these features are not random but instead have an orientation to them. Future developments in growths of this material would utilize the rotation rate to help control such formations.

The nondoped floating zone crystals are a yellowish-green color, similar to the starting powder. This is in stark contrast to dark crystals grown using the flux method as seen in Figure 1c. The origin of color often gives us insight into the vacancies and off-stoichiometries present in a material.<sup>35</sup> For PbTiO<sub>3</sub>, this color change to black has been found to occur when large amounts of excess PbO are used for the flux, with such color centers also studied computationally.<sup>36,37</sup> Our experiment supports this hypothesis on the origin of the dark color, as no excess PbO was used for the floating zone growth.

Such color differences would suggest that the vacancies involved in these samples are highly impacted by the synthesis method. A flux growth technique requires the material to stay at high temperatures for long periods of time to slowly cool and crystallize. Even though the use of excess PbO as the flux reduces the melting point, there is still an issue of PbO evaporation as evidenced by the need for a double crucible. The floating zone technique uses a faster cooling rate despite its higher operating temperature. The opportunity for PbO loss should be lessened by this approach, given the other factors (applied pressure and use of laser diode heating). These two techniques are helpful comparatively in understanding the vacancies and impurities in a material (an example being SmB<sub>6</sub>) and should apply for flux growths where volatization is utilized to help induce supersaturation.  $^{38,39}$ 

**Structure.** A comparison to the solved single crystal structure for both floating zone and flux grown samples is shown in Tables 1–4. In both cases, PbTiO<sub>3</sub> crystallizes in the

Table 1. Crystallographic Parameters of the SXRD for Floating Zone Grown PbTiO<sub>3</sub>

formula				PbTiO <sub>3</sub>				
synth meth	nod		floating zone					
cryst syst				tetragonal				
space grou	p			P4mm (No	. 99)			
a (Å)				3.8981(2)	3.8981(2)			
c (Å)				4.1601(3)				
$V(Å^3)$				63.21(1)				
Z				1				
radiation				Mo Κα, λ :	= 0.71073 Å			
temp (K)				213				
abs coeff (	$mm^{-1}$ )			69.38				
F(0 0 0)				128				
reflcns collectd								
unique/internal data agreement				1662/176				
				$R_{\rm int} = 0.054$	Į.			
data/params				176/15				
goodness-c	of-fit			1.20				
U	$- F_c  /\Sigma F_o $			0.020				
$R_{\rm w}(F^2) = \left[\Sigma w (F_{\rm o}^2 - F_{\rm c}^2)^2 / \Sigma w (F_{\rm o}^2)^2\right]^{1/2}$				0.047				
largest diff peak/hole				2.55/-1.80	e Å <sup>-3</sup>			
W	yckoff position	x (Å)	y (Å)	z (Å)	$U_{\rm iso}~({\rm \AA}^2)$			
Pb	1a	0	0	0	0.00879(16)			
Ti	1b	0.5	0.5	0.537(2)	0.0067(14)			
O1	1b	0.5	0.5	0.119(3)	0.010(2)			
O2	2c	0.5	0	0.618(2)	0.0089(15)			

Table 2. Anisotropic Displacement Parameters Based on the Floating Zone Grown Refined PbTiO<sub>3</sub> Structure

	$U_{11}$ (Å <sup>2</sup> )	$U_{22}$ (Å <sup>2</sup> )	$U_{33}  ({\rm \AA}^2)$	$U_{12} = U_{13} = U_{23}  (\mathring{A}^2)$
Pb	0.00835(17)	0.00835(17)	0.0097(3)	0
Ti	0.00446(6)	0.00446(6)	0.011(5)	0
O1	0.009(3)	0.009(3)	0.011(5)	0
O2	0.013(4)	0.003(4)	0.011(3)	0

Table 3. Crystallographic Parameters of the SXRD for Flux Grown PbTiO<sub>3</sub>

$\begin{array}{cccccccccccccccccccccccccccccccccccc$	form	ula	$PbTiO_3$							
$\begin{array}{c ccccccccccccccccccccccccccccccccccc$	synt	n method	flux							
$\begin{array}{cccccccccccccccccccccccccccccccccccc$	cryst	syst	tetragonal	tetragonal						
$\begin{array}{c ccccccccccccccccccccccccccccccccccc$	spac	e group			P4mm (No	o. 99)				
$\begin{array}{c ccccccccccccccccccccccccccccccccccc$	a (Å	.)			3.8969(1)	3.8969(1)				
$ \begin{array}{c ccccccccccccccccccccccccccccccccccc$	c (Å	)			4.1558(2)	4.1558(2)				
radiation $ \begin{tabular}{lllllllllllllllllllllllllllllllllll$	V (A	$\Lambda^3$ )			63.11 (1)					
$\begin{array}{cccccccccccccccccccccccccccccccccccc$	Z				1	1				
abs coeff (mm <sup>-1</sup> ) 69.50 $F(0\ 0\ 0) = 128$ reflens colletd $ \begin{array}{c ccccccccccccccccccccccccccccccccccc$	radia	ition			Μο Κα, λ	= 0.71073 Å				
$ \begin{array}{c ccccccccccccccccccccccccccccccccccc$	temp	(K)			213					
$\begin{tabular}{ c c c c c c c c c c c c c c c c c c c$	abs	coeff (mm <sup>-1</sup> )			69.50	69.50				
$\begin{array}{c ccccccccccccccccccccccccccccccccccc$	F(0	0 0)			128					
$\begin{array}{cccccccccccccccccccccccccccccccccccc$	reflc	ns collctd								
$\begin{array}{cccccccccccccccccccccccccccccccccccc$	uniq	ue/internal data agr	1911/176							
$\begin{array}{cccccccccccccccccccccccccccccccccccc$			$R_{\rm int} = 0.07$	1						
$R = \Sigma   F_o  -  F_c  /\Sigma  F_o  \qquad 0.013$ $R_w(F^2) = \left[\Sigma w(F_o^2 - F_c^2)^2/\Sigma w(F_o^2)^2\right]^{1/2} \qquad 0.029$ largest diff peak/hole  0.966/-1.244 e Å <sup>-3</sup> $Wyckoff position \qquad x (Å) \qquad y (Å) \qquad z (Å) \qquad U_{iso} (Å^2)$ Pb 1a 0 0 0 0.00782(15)	data	/params	176/16							
$\begin{array}{llll} R_{\rm w}(F^2) = [\Sigma w(F_{\rm o}^2 - F_{\rm c}^2)^2 / \Sigma w(F_{\rm o}^2)^2]^{1/2} & 0.029 \\ {\rm largest~diff~peak/hole} & 0.966/-1.244~e~{\rm \AA}^{-3} \\ & & & & & & & & & & & & & & & \\ Wyckoff~position & x~({\rm \AA}) & y~({\rm \AA}) & z~({\rm \AA}) & U_{\rm iso}~({\rm \AA}^2) \\ {\rm Pb} & 1a & 0 & 0 & 0 & 0.00782(15) \\ \end{array}$	good	lness-of-fit			1.12					
largest diff peak/hole $0.966/-1.244 \text{ e Å}^{-3}$ Wyckoff position $x$ (Å) $y$ (Å) $z$ (Å) $U_{iso}$ (Ų)  Pb 1a 0 0 0 0.00782(15)	R =	$\Sigma   F_{o}  -  F_{c}  /\Sigma  F_{o} $			0.013	0.013				
Wyckoff position $x$ (Å) $y$ (Å) $z$ (Å) $U_{iso}$ (Ų)           Pb         1a         0         0         0         0.00782(15)	$R_{\rm w}(F^2) = \left[\Sigma w (F_{\rm o}^2 - F_{\rm c}^2)^2 / \Sigma w (F_{\rm o}^2)^2\right]^{1/2}$				0.029					
Pb 1a 0 0 0 0.00782(15)	large	st diff peak/hole	$0.966/-1.244 \text{ e Å}^{-3}$							
. ,		Wyckoff position	x (Å)	y (Å)	z (Å)	$U_{\rm iso}~({\rm \AA}^2)$				
T: 11 0.5 0.5 0.5202(12) 0.0051(0)	Pb	1a	0	0	0	0.00782(15)				
11 16 0.5 0.5 0.5382(12) 0.0051(8)	Ti	1b	0.5	0.5	0.5382(12)	0.0051(8)				
O1 1b 0.5 0.5 0.113(2) 0.0084(16)	O1	1b	0.5	0.5	0.113(2)	0.0084(16)				
O2 2c 0.5 0 0.6178(14) 0.0060(10)	O2	2c	0.5	0	0.6178(14)	0.0060(10)				

Table 4. Anisotropic Displacement Parameters Based on the Flux Grown Refined PbTiO $_3$  Structure

	$U_{11}$ (Å <sup>2</sup> )	$U_{22}$ (Å $^2$ )	$U_{33}$ (Å <sup>2</sup> )	$U_{12} = U_{13} = U_{23}$ $(\mathring{A}^2)$
Pb	0.00846(16)	0.00846(16)	0.00654(19)	0
Ti	0.0043(5)	0.0043(5)	0.007(3)	0
O1	0.010(3)	0.010(3)	0.004(3)	0
O2	0.004(3)	0.007(3)	0.007(2)	0

P4mm space group below its Curie temperature, above which it transforms to the cubic  $Pm\overline{3}m$  phase. Like other ferroelectric perovskites such as BaTiO<sub>3</sub>, this cubic to tetragonal transition is an example of negative thermal expansion. Unlike BaTiO<sub>3</sub> however, this material exhibits no further distortion in structure upon cooling. In comparison of the unit cell volume, there is very little contraction (99.84(2)%) in the flux method compared to the floating zone method.

Another useful comparison obtained from the diffraction data is the peak width in PXRD. This can be utilized to understand some of the strain present in the grown crystals. A common method is the Williamson—Hall analysis as follows:

$$\beta \cos \theta = \frac{k\lambda}{\tau} + \sin \theta$$

where  $\beta$  corresponds to the full width at half-maximum (FWHM) of the diffraction peaks,  $\theta$  is the location of the diffraction peak in radians, k is the Scherrer constant,  $\lambda$  is the operating wavelength of the X-ray source, and  $\tau$  corresponds to the crystallite size. While there are a variety of instrumental factors that affect such an analysis, one can still make relative comparisons between crystals. This analysis shows a negative slope for both crystals, with the peak width being larger for the flux grown crystals by a factor of  $\sim 2$  (shown in Figure 3). Visualization of the anisotropic displacement parameters in Figure 4a for the floating zone grown sample shows "pancake"shaped ellipsoids on the O2 site perpendicular to the Ti-O2 bond. Such values should be interpreted cautiously due to the small mass of O compared to Ti/Pb, but such behavior has been seen in previous single crystal solutions of PbTiO<sub>3</sub>. These shape effects can be illuminating to the dynamic and static displacements of the atoms. 41 This type of behavior has occurred before in lone pair displaced materials as well as pyrochlores in general because of tetrahedral tilting. 42,43 The Ti ellipsoid is also elongated along the c-axis, suggesting this could be related to the displacement of the Ti atoms in the octahedral center. Interestingly, these features differ for the flux grown sample shown in Figure 4b, where the elongation on the  $O_2$  occurs along the Ti $-O_2$  bond, with the O1 atoms showing flattening perpendicular to the Ti-O1 bond. Further experiments involving single crystal neutron diffraction would be helpful to better contrast O with Pb/Ti for thermal parameters and occupancy, given the color centers in the flux grown crystals.

To better quantify any oxygen deficiencies in the samples, annealing experiments under  $O_2(g)$  flow were performed with TGA/DTA, as shown in Figure 5a. Both samples gain some amount of mass after a long period of annealing, but the mass gain for the flux grown samples is larger, as expected from the darker color. This is seen in the initial heating and once held at 800  $^{\circ}$ C, shown in the inset of Figure 5a. Before calculating the oxygen stoichiometry, one must consider the type of vacancy pair that is occurring. As proposed in a previous work, the use of excess PbO would generate Ti–O deficiency, written in Kröger–Vink notation 44

$$xPbO + (1 - x)PbTiO_3 \rightarrow V_{Ti}'''' + 2V_O^{\circ \circ} + PbTi_{1-x}O_{3-2x}$$

while the floating zone method would have oxygen vacancies occurring as

$$PbTiO_3 \rightarrow V''_{Pb} + V_O^{\circ \circ} + Pb_{1-x}TiO_{3-x} + xPbO(g)$$

due to PbO loss (supported by the presence of  $TiO_2$  in the traveling zone at the end of the growth measured by PXRD).<sup>36</sup> This leads to a calculation of Pb $Ti_{0.881}O_{2.761}$  and Pb $_{0.989}TiO_{2.989}$  for flux and floating zone, respectively. Both sets of samples demonstrate an endothermic transition upon heating (seen in Figure 5b). This corresponds to the tetragonal—cubic transition that occurs at T = 482 °C and T = 481 °C for the floating zone and flux sample, respectively. This slight difference in the transition could be due to an effect of the off-stoichiometry of the two samples. No change in phase is observed in PXRD of samples after TGA/DTA measurements.

**Physical Properties.** Heat capacity measurements are a useful way to examine the disorder and displacement in lone pair sterically active materials. Previous reports of the low temperature specific heat of undoped PbTiO<sub>3</sub> indicate a Schottky anomaly at low temperatures and a large broad peak represented as an Einstein oscillator that is generally present in

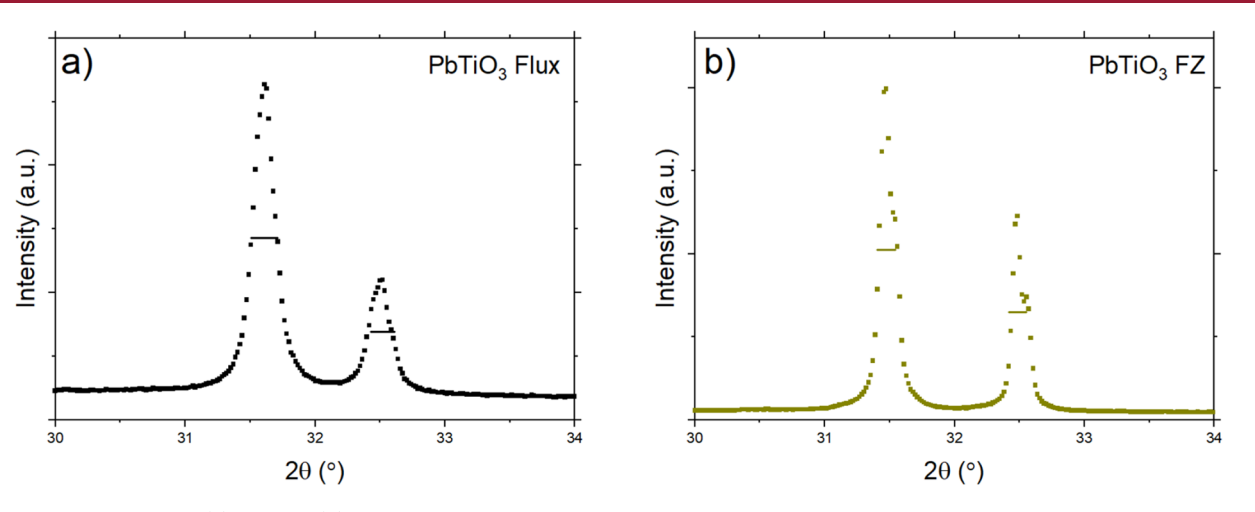


Figure 3. PXRD pattern for (a) flux and (b) floating zone crystals where the FWHM is denoted using a solid line that shows more strain present in the flux grown crystal.

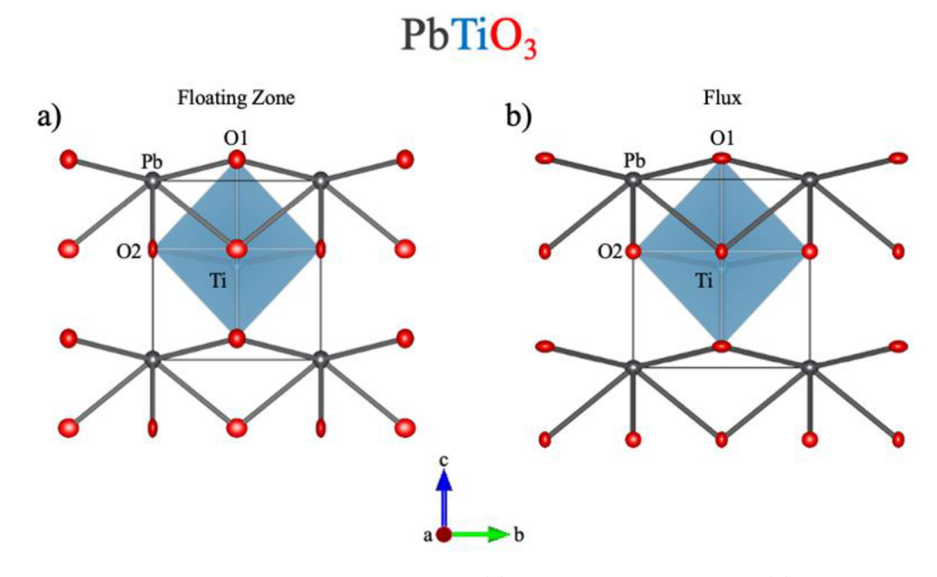


Figure 4. Visualizations of the solved crystal structure of PbTiO<sub>3</sub> for (a) floating zone grown and (b) flux grown crystals. The anisotropic displacement parameters are displayed at 80% probability.

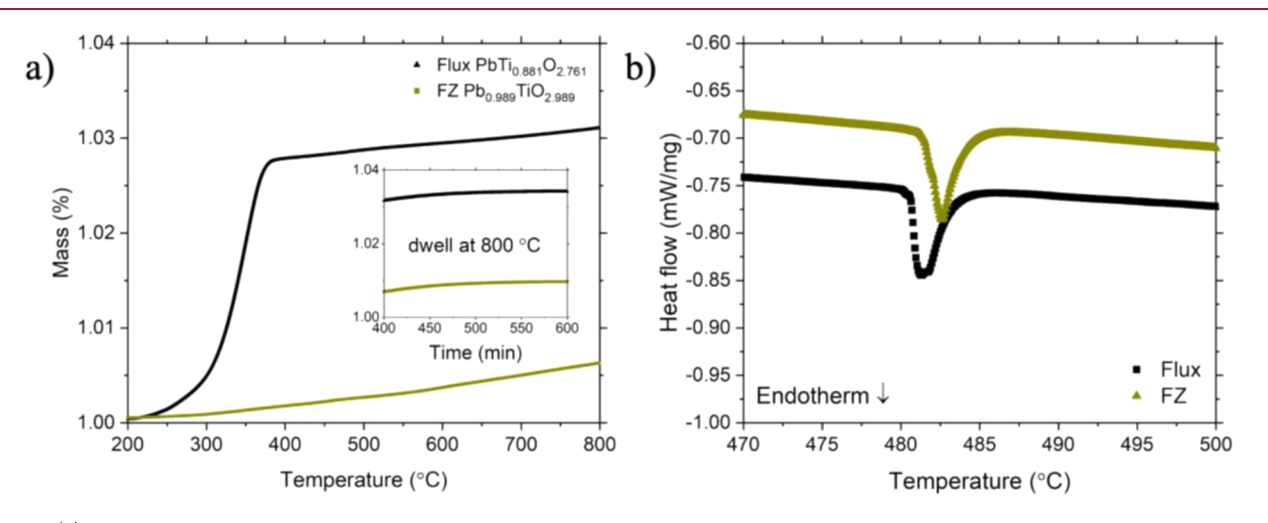
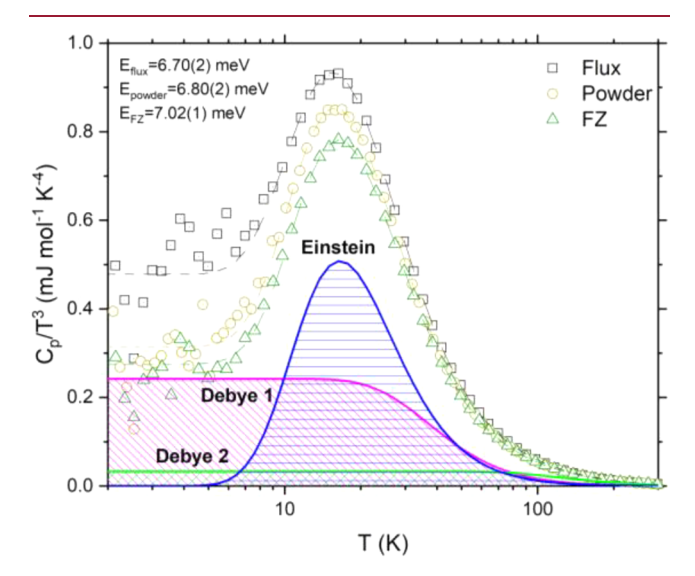


Figure 5. (a) Comparison using TGA of the uptake in oxygen upon annealing for both samples of PbTiO<sub>3</sub>. Samples grown using PbO flux demonstrate a greater amount of oxygen vacancies. Inset shows the saturation in mass once held at 800 °C. (b) Tetragonal—cubic transition for crystals grown by flux and floating zone.

ferroelectric perovskites. 46,47 This localized optical mode results from the Pb lone pair off-centering and second order Jahn–Teller distorted Ti atoms. 48 Figure 6 shows the data also



**Figure 6.** Heat capacity plotted as  $C_p/T^3$  vs  $\log(T)$  to show the presence of a broad peak at low temperatures. All data sets were fit with a series of two Debye and one Einstein mode.

plotted as  $C_p/T^3$  vs  $\log(T)$  to emphasize these features. In comparison to the data reported by Lawless et al., there is little to no upturn at low temperatures in our data coming from a Schottky term, proposed to exist due to PbO-loss disorder. Both samples' Einstein peak are similar in width and intensity in accordance with the scale of the data.

As the presence of large broad peaks can give insight into the disorder present in the sample, the heat capacity data were fit to a series of Debye and Einstein modes to model the phonon behavior between samples. Purchased PbTiO $_3$  powder used as starting material was also measured for comparison. To focus on the high temperature features, the data were fit above  $T \sim 8$  K. The terms are as follows:

$$\begin{split} C_{\text{Debye}} &= 9sR \bigg(\frac{T}{\theta_{\text{D}}}\bigg)^3 \int_0^{\theta_{\text{D}}/T} \frac{(\theta/T)^4 \mathrm{e}^{(\theta/T)}}{[\mathrm{e}^{(\theta/T)}-1]^2} \, \mathrm{d}\bigg(\frac{\theta}{T}\bigg) \\ C_{\text{Einstein}} &= 3sR \bigg(\frac{\theta_{\text{E}}}{T}\bigg)^2 \frac{\mathrm{e}^{(\theta_{\text{E}}/T)}}{[\mathrm{e}^{(\theta_{\text{E}}/T)}-1]^2} \\ C_{\text{total}} &= C_{\text{Debye}1} + C_{\text{Debye}2} + C_{\text{Einstein}} \end{split}$$

where s relates to the number of oscillators per formula unit,  $\theta_{\rm D}$  is the Debye temperature, and  $\theta_{\rm E}$  corresponds to the Einstein temperature.

In determining the correct number of fitting parameters, a comparison in the quality of fit was performed using a combination of Debye and Einstein modes. It was found that using 2 Debye and 1 Einstein mode best modeled the data by

adding closest to the correct number of oscillators (5) rather than overfitting (too many Einstein terms) or underfitting (too few Debye terms). This is further supported in comparison of the  $R^2$  values between fits. The resulting terms are represented in Table 5, with uncertainties derived from the standard error of the fit.

The sum of the oscillators should add up to the total number of atoms per formula unit, five in the case of  $PbTiO_3$ . In our fits, the powder adheres best to this number, with the floating zone oscillator number slightly overshooting and the flux sample overshooting by a larger amount. All fits reach similar values for their Debye and Einstein temperatures. Scaling by the oscillators leads the powder and floating zone samples' Einstein peaks to have similar intensity, but the flux sample's peak grows in size.

Figure 7 shows the data plotted as  $C_p/T$  vs  $T^2$  to emphasize the presence of a term linear in  $T^2$  at low temperatures. At low

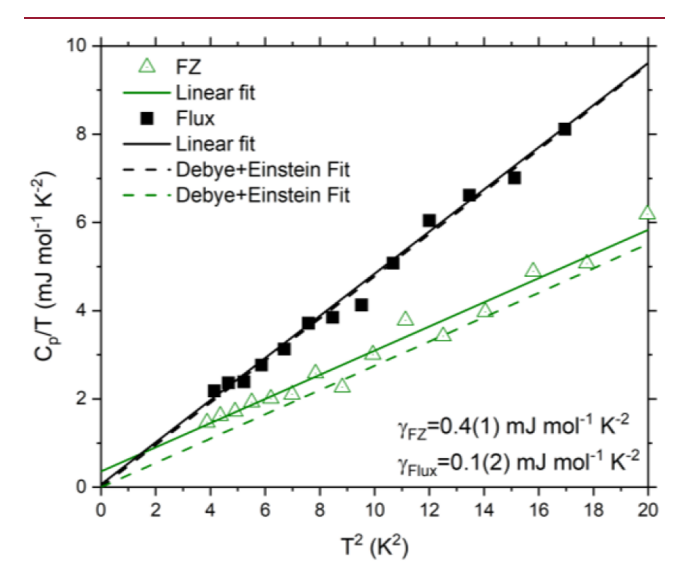


**Figure 7.** Low temperature region of heat capacity for both sets of crystals, showing a linear contribution, which can be fit to a simple linear model. The sample data can also be fit using the full Debye and Einstein terms derived from the  $C_p/T^3$  data, showing the energy of the Einstein term correlates to the "slope" of the seemingly linear data.

temperatures ( $T \ll \theta_{\rm D}/50$ ) the heat capacity can be approximated by the following equation:

$$C_{\nu} \approx \gamma T + \beta_3 T^3$$

where  $\gamma$  is the electronic contribution and  $\beta_3$  corresponds to the phonon contribution. The heat capacity fit modeled from the full Debye and Einstein modes also shows approximately linear behavior when plotted this way. While one would expect an electronic contribution to show up for metals, this linear relationship holds true for many insulators as well. A variety of phenomena such as 1D spin chains, structural disorder, and lattice vacancies has been known to produce such behavior. The linear fits to the data give us  $\gamma$  values of 0.4(1) mJ

Table 5. Fitting Parameters to the C<sub>D</sub>/T<sup>3</sup> Data for Flux and Floating Zone Crystal and Starting Powder

	$s_{\mathrm{D1}}$ (oscillator strength/formula unit)	$\theta_{\mathrm{D1}}\left(\mathrm{K}\right)$	$s_{\mathrm{D2}}$	$\theta_{D2}$ (K)	$s_{\rm E}$	$\theta_{\rm E}$ (K)	sum of oscillators
flux	0.93(2)	161(2)	4.09(3)	593(6)	0.420(6)	77.7(2)	5.44(3)
FZ	0.76(1)	183(2)	3.84(3)	608(5)	0.515(5)	81.4(1)	5.12(3)
powder	0.80(2)	177(2)	3.64(3)	597(7)	0.501(6)	78.9(2)	4.94(4)

 $\mathrm{mol}^{-1}~\mathrm{K}^{-2}$  and 0.1(2) mJ  $\mathrm{mol}^{-1}~\mathrm{K}^{-2}$  for the floating zone and flux samples, respectively. While small, these values are not unusual in scale for such insulating oxides. The linear term can be correlated to the number vacancies according to

$$\gamma_{\rm calc} = c n_{\rm vac}$$

where c is the correlation value based on the distribution of the energy gap from the Schottky contribution of the vacancies present. According to this relation the number of vacancies for the flux sample should be smaller, contradicting the TGA/DTA data collected. The ordering of these vacancies can have an impact on the predictability of this theory, which would indicate the presence of defect clustering for these samples. <sup>55</sup>

Thus, the more exotic phenomenon for the proposed linear term is ruled out by plotting the combined Debye and Einstein phonon contribution. One can see this fits the data almost identically to the linear fit. Given that both fits have a general phonon contribution, the addition of an Einstein oscillator best explains the linearity at low temperatures when plotted this way. The difference in energy between the two samples' Einstein terms best explains the proposed difference in slope between the samples at low temperature. This shows that when considering the presence of a linear contribution in insulators, the disorder present from off-centering can serve as a more reasonable explanation compared to rarer, exotic behavior. S6

To investigate potential onset of magnetic behavior, magnetization as a function of applied magnetic field measurements were performed on the flux grown sample, floating zone sample, and a second floating zone sample doped with 1% Er at room temperature. Magnetic moments were seen for both Er-doped and flux grown samples, while the undoped floating zone sample showed diamagnetic behavior as seen in Figure 8. Of the three, the flux sample also showed the presence of slight hysteresis at room temperature with a coercive field of approximately 50 Oe, shown in Figure 8 inset.

Given the hysteresis shown in the M vs H curve, this leads one to wonder, where is the ferromagnetic signal coming from and why is it only present in the flux grown sample? The

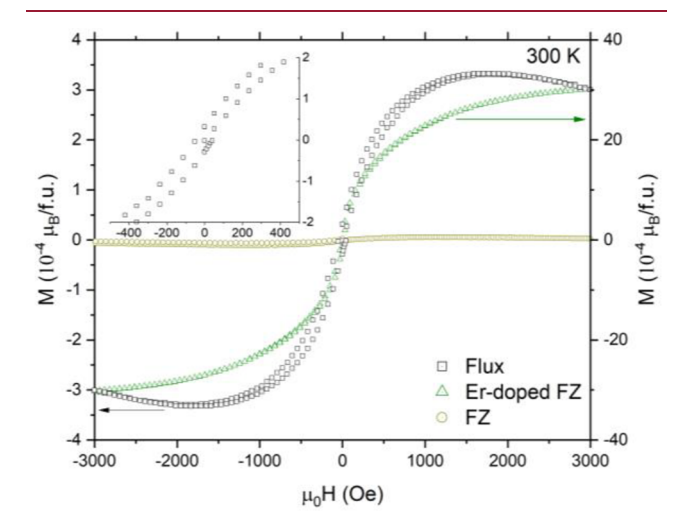


**Figure 8.** Presence of weak hysteresis in magnetization as a function of field for flux grown (left) crystals of PbTiO<sub>3</sub>. The saturation in moment is quickly dispersed upon application of higher fields and is not impacted postannealing under oxygen. This is contrasted with floating zone crystals (right showing Er-doped and inset showing the pure material).

presence of ferromagnetism in d<sup>0</sup> oxides has been met with significant (and well deserved!) skepticism as to the origin.<sup>5</sup> Previous works have predicted/reported the onset of room temperature ferromagnetism of similar magnitude in PbTiO<sub>3</sub> due to the presence of oxygen vacancies. 58-60 If this behavior was indeed due to oxygen deficiencies, measurement of an annealed sample should show a decrease in response. Measurement of annealed flux grown crystals (supported by TGA measurements) show no decrease in magnetic signal. Due to the corrosive nature of PbO as a flux, it is possible for impurities being incorporated into the crystal. Analysis of both crystal types using GDMS in Table 6 show a large impurity of Ir and Pt for the flux grown sample, likely etched off the crucible. The saturated magnetic moment can be utilized to estimate the impurity concentration. Ir<sup>4+</sup> as the magnetic dopant gives us an estimated impurity of ~190 ppm using the expected effective magnetic moment of 1  $\mu_{\rm B}/{\rm Ir}$ . The actual observed saturated moment for such Ir-containing magnetic

Table 6. Trace Elemental Analysis Performed for Both a Floating Zone and Flux Grown PbTiO<sub>3</sub> Using GDMS

element	floating zone concn (ppm wt)	flux concn (ppm wt)	element	floating zone concn (ppm wt)	flux concn (ppm wt)
Li	0.05	0.13	Ag	<50	<50
Be	< 0.01	< 0.01	Cd	<10	<10
В	27	2.4	In	binder	binder
0	matrix	matrix	Sn	120	8
F	<1	<1	Sb	4.1	1.5
Na	20	40	Te	<5	<5
Mg	280	24	I	<5	<5
Al	68	4.6	Cs	<1	<1
Si	520	10	Ba	18	12
P	140	2.4	La	1.2	1
S	25	1.8	Ce	<0.5	< 0.5
Cl	73	8.3	Pr	0.16	0.31
K	19	2.1	Nd	<0.5	12
Ca	130	170	Sm	< 0.5	< 0.5
Sc	<0.5	< 0.5	Eu	0.23	0.17
Ti	matrix	matrix	Gd	0.85	< 0.1
V	0.48	0.08	Tb	1.9	< 0.1
Cr	2.2	0.26	Dy	< 0.1	< 0.1
Mn	0.52	0.09	Ho	< 0.1	< 0.1
Fe	54	19	Er	<0.1	< 0.1
Co	71	28	Tm	< 0.1	< 0.1
Ni	3	2.1	Yb	82	0.16
Cu	6.3	0.26	Lu	<0.1	< 0.1
Zn	2.6	0.47	Hf	3.8	3.6
Ga	50	< 0.05	Ta	<10	<10
Ge	<0.5	< 0.5	W	1.6	0.67
As	< 0.05	< 0.05	Re	< 0.05	< 0.05
Se	<0.5	< 0.5	Os	< 0.05	< 0.05
Br	<0.5	< 0.5	Ir	0.09	4100
Rb	<2	<2	Pt	<5	340
Sr	320	430	Au	<1	<1
Y	17	27	Hg	<0.5	< 0.5
Zr	190	200	Tl	<0.5	< 0.5
Nb	32	110	Pb	matrix	matrix
Mo	2.5	< 0.5	Bi	52	54
Ru	< 0.1	< 0.1	Th	< 0.01	< 0.01
Rh	<1	<5	U	< 0.01	< 0.01
Pd	<50	< 50			

materials is often less, however, such as the case of  $\rm Sr_2 IrO_4$ , and using such an expected saturated moment (0.07  $\mu_B/\rm Ir$ ) gives ~2715 ppm, closer to the determined value. <sup>61,62</sup> With this evidence, we can conclude that samples grown by floating zone are not only less oxygen deficient but also have fewer impurities (via avoiding crucible contamination and the zone refinement that naturally occurs in floating zone growths). Further research can be pursued to see the impact of Ir as an intentional dopant on the magnetic order in PbTiO<sub>3</sub>.

In comparison to the flux crystals, the Er-doped sample shows an order of magnitude larger saturated moment, as expected for the large magnetic moment in  $\rm Er^{3+}$ . However, if we assume a saturation moment of  $3\times 10^{-3}$  and an effective magnetic moment of  $9.5~\mu_{\rm B}/\rm Er$ , we get a corresponding mole fraction of  $3\times 10^{-4}$ , lower than our expected doping with Er. This is due to a concentration gradient forming for the grown crystal due to the zone refining of the floating zone method before a steady state is reached. No noticeable change in color along the length of the crystal limits the magnitude of gradient expected.

## CONCLUSION

Overall, our work has demonstrated the feasibility of growing crystals of  $\mathrm{PbTiO}_3$  using the floating zone method through tuning of growth parameters as well as implementation of laser diodes as the heating source. Due to the structural transition of cubic to tetragonal upon cooling, development of large single crystals will need to be improved, although other floating zone experiments dealing with such phase transitions have found a sharper gradient helps avoid such cracking.  $^{63}$ 

A comparison between crystals grown through floating zone and flux method demonstrate key difference in how the growth technique can impact the properties of the material. Through careful analysis of the heat capacity, we can rule out linear behavior in place of a more thorough fit of the phonon modes. The floating zone grown samples demonstrate lower defects present as evidenced by GDMS analysis, the lack of magnetism present, and the quantification of O vacancies using TGA/ DTA. This reduction in defects is accomplished through the zone refinement of the inherent technique. Doping of Er (as evidenced in magnetization measurements) demonstrates the feasibility of introduction of Er for future improved multiferroic performance and quantum platforms in floating zone crystals. This work shows the capabilities of the laser floating zone technique to allow for the growth of low defect PbTiO<sub>3</sub> and can be applied more generally to volatile materials.

# ASSOCIATED CONTENT

#### **Data Availability Statement**

Raw data from the facility related to these syntheses is available at https://doi.org/10.34863/6x7g-3a87.

# **Accession Codes**

CCDC 2181876—2181877 contain the supplementary crystallographic data for this paper. These data can be obtained free of charge via <a href="www.ccdc.cam.ac.uk/data\_request/cif">www.ccdc.cam.ac.uk/data\_request/cif</a>, or by emailing <a href="data\_request@ccdc.cam.ac.uk">data\_request/cif</a>, or by contacting The Cambridge Crystallographic Data Centre, 12 Union Road, Cambridge CB2 1EZ, UK; fax: +44 1223 336033.

#### AUTHOR INFORMATION

# **Corresponding Authors**

Lucas A. Pressley — Department of Chemistry, The Johns Hopkins University, Baltimore, Maryland 21218, United States; Institute for Quantum Matter, The William H. Miller III Department of Physics and Astronomy, The Johns Hopkins University, Baltimore, Maryland 21218, United States; orcid.org/0000-0002-0765-3333; Email: lpressl3@jh.edu

Tyrel M. McQueen — Department of Chemistry, The Johns Hopkins University, Baltimore, Maryland 21218, United States; Institute for Quantum Matter, The William H. Miller III Department of Physics and Astronomy and Department of Materials Science and Engineering, The Johns Hopkins University, Baltimore, Maryland 21218, United States; orcid.org/0000-0002-8493-4630; Email: mcqueen@jhu.edu

#### **Authors**

Mekhola Sinha — Department of Chemistry, The Johns Hopkins University, Baltimore, Maryland 21218, United States; Institute for Quantum Matter, The William H. Miller III Department of Physics and Astronomy, The Johns Hopkins University, Baltimore, Maryland 21218, United States; © orcid.org/0000-0001-8776-4721

Hector K. Vivanco – Department of Chemistry, The Johns Hopkins University, Baltimore, Maryland 21218, United States; Institute for Quantum Matter, The William H. Miller III Department of Physics and Astronomy, The Johns Hopkins University, Baltimore, Maryland 21218, United States

Juan Chamorro – Department of Chemistry, The Johns Hopkins University, Baltimore, Maryland 21218, United States; Institute for Quantum Matter, The William H. Miller III Department of Physics and Astronomy, The Johns Hopkins University, Baltimore, Maryland 21218, United States

Sujit Das — Department of Materials Science and Engineering, University of California, Berkeley, California 94720, United States; Present Address: Material Research Centre, Indian Institute of Science, Bangalore, 560012, India; orcid.org/0000-0001-9823-0207

Ramamoorthy Ramesh — Department of Materials Science and Engineering and Department of Electrical Engineering and Computer Sciences, University of California, Berkeley, California 94720, United States

Complete contact information is available at: https://pubs.acs.org/10.1021/acs.cgd.2c00716

#### Notes

The authors declare no competing financial interest.

#### ACKNOWLEDGMENTS

This work was funded by the Platform for the Accelerated Realization, Analysis, and Discovery of Interface Materials (PARADIM), a National Science Foundation Materials Innovation Platform (Grant NSF DMR-2039380). The MPMS was funded by the National Science Foundation, Division of Materials Research, Major Research Instrumentation Program, under Award 1828490. We thank Dr. Maxime Siegler for helping with single crystal data collection.

## REFERENCES

- (1) Yang, X.; Zhou, Z.; Nan, T.; Gao, Y.; Yang, G. M.; Liu, M.; Sun, N. X. Recent Advances in Multiferroic Oxide Heterostructures and Devices. J. Mater. Chem. C 2016, 4, 234–243.
- (2) Lu, C.; Hu, W.; Tian, Y.; Wu, T. Multiferroic Oxide Thin Films and Heterostructures. *Appl. Phys. Rev.* **2015**, *2*, 021304.
- (3) Eerenstein, W.; Mathur, N. D.; Scott, J. F. Multiferroic and Magnetoelectric Materials. *Nature* **2006**, 442, 759–765.
- (4) Fiebig, M.; Lottermoser, T.; Meier, D.; Trassin, M. The Evolution of Multiferroics. *Nat. Rev. Mater.* **2016**, *1*, 16046.
- (5) Rai, R.; Mishra, S. K.; Singh, N. K.; Sharma, S.; Kholkin, A. L. Preparation, Structures, and Multiferroic Properties of Single-Phase BiRFeO<sub>3</sub>, R = La and Er Ceramics. *Curr. Appl. Phys.* **2011**, *11* (3), 508–512.
- (6) Le Dantec, M.; Rančić, M.; Lin, S.; Billaud, E.; Ranjan, V.; Flanigan, D.; Bertaina, S.; Chanelière, T.; Goldner, P.; Erb, A.; Liu, R. B.; Estève, D.; Vion, D.; Flurin, E.; Bertet, P. Twenty-Three–Millisecond Electron Spin Coherence of Erbium Ions in a Natural-Abundance Crystal. *Sci. Adv.* **2021**, *7* (51), eabj9786.
- (7) Ali Saha, R.; Halder, A.; Fu, D.; Itoh, M.; Saha-Dasgupta, T.; Ray, S. The Critical Role of Stereochemically Active Lone Pair in Introducing High Temperature Ferroelectricity. *Inorg. Chem.* **2021**, *60* (6), 4068–4075.
- (8) Zhang, S.; Li, F. High Performance Ferroelectric Relaxor-PbTiO<sub>3</sub> Single Crystals: Status and Perspective. *J. Appl. Phys.* **2012**, *111*, 031301.
- (9) Bhatti, H. S.; Hussain, S. T.; Khan, F. A.; Hussain, S. Synthesis and Induced Multiferroicity of Perovskite PbTiO<sub>3</sub>; a Review. *Appl. Surf. Sci.* **2016**, *367*, 291–306.
- (10) Grabmaier, B. C. PbTiO<sub>3</sub> Grown from the Melt. Ferroelectrics 1976, 13 (1), 501–503.
- (11) Gelabert, M. C.; Laudise, R. A.; Riman, R. E. Phase Stability, Solubility and Hydrothermal Crystal Growth of PbTiO<sub>3</sub>. *J. Cryst. Growth* **1999**, 197 (1–2), 195–203.
- (12) Harada, K.; Shimanuki, S.; Kobayashi, T.; Saitoh, S.; Yamashita, Y. Crystal Growth and Electrical Properties of Pb-((Zn<sub>1/3</sub>Nb<sub>2/3</sub>)<sub>0.91</sub>Ti<sub>0.09</sub>)O<sub>3</sub> Single Crystals Produced by Solution Bridgman Method. *J. Am. Ceram. Soc.* **1998**, *81* (11), 2785–2788.
- (13) Xu, J.; Fan, S.; Lu, B.; Tong, J.; Zhang, A. Seeded Growth of Relaxor Ferroelectric Single Crystals Pb[(Zn<sub>1/3</sub>Nb<sub>2/3</sub>)<sub>0.91</sub>Ti<sub>0.09</sub>O<sub>3</sub> by the Vertical Bridgman Method. *Jpn. J. Appl. Phys.* **2002**, *41*, 7000–7002.
- (14) Zhang, S.; Rehrig, P. W.; Randall, C.; Shrout, T. R. Crystal Growth and Electrical Properties of  $Pb(Yb_{1/2}Nb_{1/2})O_3$ -PbTiO<sub>3</sub> Perovskite Single Crystals. *J. Cryst. Growth* **2002**, 234 (2–3), 415–420.
- (15) Lee, H. Y. Development of High-Performance Piezoelectric Single Crystals by Using Solid-State Single Crystal Growth (SSCG) Method. In *Handbook of Advanced Dielectric, Piezoelectric and Ferroelectric Materials*; Woodhead, 2008; pp 158–172.
- (16) Sun, B. N.; Huang, Y.; Payne, D. A. Growth of Large PbTiO<sub>3</sub> Crystals by a Self-Flux Technique. *J. Cryst. Growth* **1993**, 128 (1–4), 867–870.
- (17) Burnett, T. L.; Comyn, T. P.; Bell, A. J. Flux Growth of BiFeO<sub>3</sub>-PbTiO<sub>3</sub> Single Crystals. *J. Cryst. Growth* **2005**, 285 (1–2), 156–161.
- (18) Kakuta, K.; Tsurumi, T.; Fukunaga, O. Dielectric Property of Flux-Grown PbTiO<sub>3</sub> Single Crystal. *Jpn. J. Appl. Phys.* **1995**, *34*, 5341.
- (19) Mabud, S. A.; Glazer, A. M. Lattice Paramters and Birefringence in PbTiO<sub>3</sub> Single Crystals. *J. Appl. Crystallogr.* **1979**, 12, 49–53.
- (20) Buehler, E. Contribution to the Floating Zone Refining of Silicon. Rev. Sci. Instrum. 1957, 28 (6), 453–460.
- (21) Maffei, N.; Rossetti, G. A., Jr. Float-Zone Growth and Properties of Ferroelectric Lead Titanate. *J. Mater. Res.* **2004**, *19* (3), 827–833.
- (22) Ito, T.; Ushiyama, T.; Yanagisawa, Y.; Tomioka, Y.; Shindo, I.; Yanase, A. Laser-Diode-Heated Floating Zone (LDFZ) Method Appropriate to Crystal Growth of Incongruently Melting Materials. *J. Cryst. Growth* **2013**, 363, 264–269.

- (23) Sinha, M.; Pearson, T. J.; Reeder, T. R.; Vivanco, H. K.; Freedman, D. E.; Phelan, W. A.; McQueen, T. M. Introduction of Spin Centers in Single Crystals of Ba<sub>2</sub>CaWO<sub>6-∂</sub>. *Phys. Rev. Mater.* **2019**, *3*, 125002.
- (24) Berry, T.; Pressley, L. A.; Phelan, W. A.; Tran, T. T.; McQueen, T. M. Laser Enhanced Single Crystal Growth of Non-Symmorphic Materials: Applications to an Eight-Fold Fermion Candidate. *Chem. Mater.* **2020**, 32, 5827–5834.
- (25) Berry, T.; Bernier, S.; Auffermann, G.; McQueen, T. M.; Phelan, W. A. Laser Floating Zone Growth of SrVO<sub>3</sub> Single Crystals. *J. Cryst. Growth* **2022**, *583*, 126518.
- (26) Sinha, M.; Vivanco, H. K.; Wan, C.; Siegler, M. A.; Stewart, V. J.; Pogue, E. A.; Pressley, L. A.; Berry, T.; Wang, Z.; Johnson, I.; Chen, M.; Tran, T. T.; Phelan, W. A.; McQueen, T. M. Twisting of 2D Kagome Sheets in Layered Intermetallics. *ACS Central Science* 2021, 7, 1381–1390.
- (27) Scudder, M. R.; He, B.; Wang, Y.; Rai, A.; Cahill, D. G.; Windl, W.; Heremans, J. P.; Goldberger, J. E. Highly Efficient Transverse Thermoelectric Devices with Re<sub>4</sub>Si<sub>7</sub> Crystals. *Energy Environ. Sci.* **2021**, *14*, 4009–4017.
- (28) Straker, M.; Chauhan, A.; Sinha, M.; Phelan, W. A.; Chandrashekhar, M. V. S.; Hemker, K. J.; Marvel, C.; Spencer, M. Growth of High Purity Zone-Refined Boron Carbide Single Crystals by Laser Diode Floating Zone Method. *J. Cryst. Growth* **2020**, *543*, 125700.
- (29) Farrugia, L. J. WinGX Suite for Small-Molecule Single-Crystal Crystallography. *J. Appl. Crystallogr.* **1999**, 32, 837–838.
- (30) Clark, R. C.; Reid, J. S. The Analytical Calculation of Absorption in Multifaceted Crystals. *Acta Crystallogr.* **1995**, *A51*, 887–897.
- (31) Phelan, W. A.; Zahn, J.; Kennedy, Z.; McQueen, T. M. Pushing Boundaries: High Pressure, Supercritcal Optical Floating Zone Materials Discovery. *J. Sol. St. Chem.* **2019**, *270*, 705–709.
- (32) Dabkowska, H. A.; Dabkowski, A. B. Crystal Growth of Oxides by Optical Floating Zone Technique. In *Springer Handbook of Crystal Growth*; Springer: Heidelberg, Germany, 2010; pp 367–390. DOI: 10.1007/978-3-540-74761-1\_12.
- (33) Koohpayeh, S. M.; Fort, D.; Abell, J. S. The Optical Floating Zone Technique: A Review of Experimental Procedures with Special Reference to Oxides. *Progress in Crystal Growth and Characterization of Materials* **2008**, 54 (3–4), 121–137.
- (34) Koohpayeh, S. M.; Wen, J.-J.; Trump, B. A.; Broholm, C. L.; McQueen, T. M. Synthesis, Floating Zone Crystal Growth and Characterization of the Quantum Spin Ice Pr2Zr2O7 Pyrochlore. *J. Cryst. Growth* **2014**, 402, 291–298.
- (35) Arpino, K. E.; Trump, B. A.; Scheie, A. O.; McQueen, T. M.; Koohpayeh, S. M. Impact of Stoichiometry of  $Yb_2Ti_2O_7$  on Its Physical Properties. *Phys. Rev. B* **2017**, *95*, 094407.
- (36) Wôjcik, K. The Influence of Point Defects on Selected Properties of PbTiO<sub>3</sub> Crystals. *Ferroelectrics* **1988**, *82*, 25–35.
- (37) Man, Z. Y.; Feng, X. Q. A Computer Simluation Study of Defects in PbTiO<sub>3</sub> Crystals. *Solid State Commun.* **2002**, *123* (8), 333–337.
- (38) Phelan, W. A.; Koohpayeh, S. M.; Cottingham, P.; Tutmaher, J. A.; Leiner, J. C.; Lumsden, M. D.; Lavelle, C. M.; Wang, X. P.; Hoffmann, C.; Siegler, M. A.; Haldolaarachchige, N.; Young, D. P.; McQueen, T. M. On the Chemistry and Physical Properties of Flux and Floating Zone Grown SmB<sub>6</sub> Single Crystals. *Sci. Rep.* **2016**, *6*, 20860.
- (39) Eo, Y. S.; Rakoski, A.; Sinha, S.; Mihaliov, D.; Fuhrman, W. T.; Saha, S. R.; Rosa, P. F. S.; Fisk, Z.; Hatnean, M. C.; Balakrishnan, G.; Chamorro, J. R.; Phelan, W. A.; Koohpayeh, S. M.; McQueen, T. M.; Kang, B.; Song, M.-s.; Cho, B.; Fuhrer, M. S.; Paglione, J.; Kurdak, C.iy. Bulk Transport Paths Through Defects in Floating Zone and Al Flux Grown SmB<sub>6</sub>. *Phys. Rev. Materials* **2021**, *5* (5), 055001.
- (40) Kushwaha, S. K.; Maurya, K. K.; Vijayan, N.; Kumar, B.; Bhatt, R.; Ganesamoorthy, S.; Bhagavannarayana, G. Crystalline Perfection, Raman, UV-VIS-NIR and Prism Coupler Investigations on Cz-Grown

- Pure and Zn-Doped LiNbO<sub>3</sub>. CrystEngComm 2012, 14 (9), 3297-
- (41) Yoshiasa, A.; Nakatani, T.; Nakatsuka, A.; Okube, M.; Sugiyama, K.; Mashimo, T. High-Temperature Single-Crystal X-Ray Diffraction Study of Tetragonal and Cubic Perovskite-Type PbTiO<sub>3</sub> Phases. Acta Crystallogr. B 2016, 72 (3), 381-388.
- (42) Shoemaker, D. P.; Seshadri, R.; Hector, A. L.; Llobet, A.; Proffen, T.; Fennie, C. J. Atomic Displacements in the Charge Ice Pyrochlore Bi<sub>2</sub>Ti<sub>2</sub>O<sub>6</sub>O' Studied by Neutron Total Scattering. Phys. Rev. B 2010, 81, 144113.
- (43) Trump, B. A.; Koohpayeh, S. M.; Livi, K. J. T.; Wen, J.-J.; Arpino, K. E.; Ramasse, Q. M.; Brydson, R.; Feygenson, M.; Takeda, H.; Takigawa, M.; Kimura, K.; Nakatsuji, S.; Broholm, C. L.; McQueen, T. M. Universal Geometric Frustation in Pyrochlores. Nat. Commun. 2018, 9, 2619.
- (44) Kröger, F. A.; Vink, H. J. Relations between the Concentrations of Imperfections in Crystalline Solids. In Solid State Physics; Academic Press, 1956; Vol. 3, pp 307-345. DOI: 10.1016/S0081-1947(08) 60135-6.
- (45) Trump, B. A.; McQueen, T. M. Structure, Properties, and Disorder in the New Distorted-Hollandite PbIr<sub>4</sub>Se<sub>8</sub>. J. Sol. St. Chem. **2016**, 242 (1), 112–119.
- (46) Melot, B. C.; Tackett, R.; O'Brien, J.; Hector, A. L.; Lawes, G.; Seshadri, R.; Ramirez, A. P. Large Low-Temperature Specific Heat in Pyrochlore Bi<sub>2</sub>Ti<sub>2</sub>O<sub>7</sub>. Phys. Rev. B 2009, 79, 22.
- (47) Lawless, W. N.; Nakamura, T.; Takashige, M.; Swartz, S. L. Specific Heat of Amorphous and Crystalline PbTiO3 at Low Temperatures. J. Phys. Soc. Jpn. 1983, 52 (1), 207-214.
- (48) Seshadri, R. Visualizing Lone Pairs in Compounds Containing Heavier Congeners of the Carbon and Nitrogen Group Elements. J. Chem. Sci. 2001, 113, 487-496.
- (49) Dender, D. C.; Hammar, P. R.; Reich, D. H.; Broholm, C. L.; Aeppli, G. Direct Observation of Field-Induced Incommensurate Fluctuations in a One-Dimensional S = 1/2 Antiferromagnet. Phys. Rev. Lett. 1997, 79 (9), 1750.
- (50) Haraguchi, Y.; Matsuo, A.; Kindo, K.; Hiroi, Z. Quantum Antiferromagnet Bluebellite Comprising a Maple-Leaf Lattice Made of Spin-1/2 Cu<sup>2+</sup> Ions. Phys. Rev. B 2021, 104 (17), 174439.
- (51) Tari, A. The Specific Heat of Matter at Low Temperatures; Imperial College Press: London, 2003. DOI: 10.1142/p254.
- (52) Schliesser, J. M.; Woodfield, B. F. Lattice Vacancies Responsible for the Linear Dependence of the Low-Temperature Heat Capacity of Insulating Materials. Phys. Rev. B 2015, 91 (2), 024109.
- (53) Kumagai, K.; Nakamichi, Y.; Watanabe, I.; Nakamura, Y.; Nakajima, H.; Wada, N.; Lederer, P. Linear Temperature Term of Heat Capacity in Insulating and Superconducting La-Ba-Cu-O Systems. Phys. Rev. Lett. 1988, 60 (8), 724-727.
- (54) Stephens, R. B. Low-Temperature Specific Heat and Thermal Conductivity of Noncrystalline Dielectric Solids. Phys. Rev. B 1973, 8 (6), 2896-2905.
- (55) Neilsen, G.; Rosen, P. F.; Dickson, M. S.; Popovic, M.; Schliesser, J.; Hansen, L. D.; Navrotsky, A.; Woodfield, B. F. Quantifying Oxygen Vacancies in Neodymium and Samarium Doped Ceria from Heat Capacity Measurements. Acta Mater. 2020, 188, 740-744.
- (56) Chamorro, J. R.; McQueen, T. M.; Tran, T. T. Chemistry of Quantum Spin Liquids. Chem. Rev. 2021, 121 (5), 2898-2934.
- (57) Coey, J. M. D. Magnetism in D<sup>0</sup> Oxides. Nat. Mater. 2019, 18,
- (58) Shimada, T.; Uratani, Y.; Kitamura, T. Vacancy-Driven Ferromagnetism in Ferroelectric PbTiO3. Appl. Phys. Lett. 2012, 100, 162901.
- (59) Xu, T.; Shimada, T.; Araki, Y.; Wang, J.; Kitamura, T. Multiferroic Domain Walls in Ferroelectric PbTiO3 with Oxygen Deficiency. Nano Lett. 2016, 16 (1), 454-458.
- (60) Zhang, Z.; Hu, J.; Xu, Z.; Qin, H.; Sun, L.; Gao, F.; Zhang, Y.; Jiang, M. Room-Temperature Ferromagnetism and Ferroelectricity in Nanocrystalline PbTiO<sub>3</sub>. Solid State Sci. 2011, 13 (7), 1391–1395.

- (61) Cao, G.; Bolivar, J.; McCall, S.; Crow, J. E.; Guertin, R. P. Weak Ferromagnetism, Metal-to-Nonmetal Transition, and Negative Differential Resistivity in Single-Crystal Sr<sub>2</sub>IrO<sub>4</sub>. Phys. Rev. B 1998, 57 (18), R11039.
- (62) Kim, B. J.; Ohsumi, H.; Komesu, T.; Sakai, S.; Morita, T.; Takagi, H.; Arima, T. Phase-Sensitive Observation of a Spin-Orbital Mott State in Sr<sub>2</sub>IrO<sub>4</sub>. Science 2009, 323 (5919), 1329-1332.
- (63) Peets, D. C.; Kim, J.; Reehuis, M.; Dosanjh, P.; Keimer, B. Floating Zone Growth of Large Single Crystals of SrFeO<sub>3-ð</sub>. J. Cryst. Growth 2012, 361, 201-205.

# **□** Recommended by ACS

Controlled Growth of Semiconductor Alloy/Ferromagnetic Insulator (GeBi/Bi:Thulium Iron Garnet (TmIG)) Spin Heterojunction and Development of Quantum Logic Device

Shuaicheng Liu, Huaiwu Zhang, et al.

MAY 19, 2023

ACS APPLIED ELECTRONIC MATERIALS

READ **C** 

# Hole and Electron Doping Outcomes in Bi<sub>2</sub>YO<sub>4</sub>Cl

Jyoti Pandey, Rajamani Nagarajan, et al.

JUNE 02, 2023

INORGANIC CHEMISTRY

READ **C** 

# A Quintuple-Layered Binary Chalcogenide Sb, Te, Single **Crystal and Its Transport Properties for Thermoelectric Applications**

Arumugam Raja, Ramasamy Perumalsamy, et al.

JULY 28, 2022

ACS OMEGA

READ **C** 

# Reliable BiI<sub>3</sub>-Based Resistive Random-Access Memory Devices with a High On/Off Ratio

Mei-Hsin Chen, Ju-Feng Cheng, et al.

DECEMBER 20, 2022

ACS APPLIED ELECTRONIC MATERIALS

READ **C** 

Get More Suggestions >